Energy Advances

ROYAL SOCIETY OF CHEMISTRY

COMMUNICATION

View Article Online
View Journal | View Issue

Cite this: *Energy Adv.*, 2024, 3, 774

Received 2nd October 2023,
Accepted 29th February 2024

DOI: 10.1039/d3ya00489a

rsc.li/energy-advances

A quick and effective strategy for the synthesis of $Ti_3C_2T_x$ *via* electrochemical method†

Shrabani De,[a] Sourav Acharya,[a] Satyanarayan Sahoo [b] and Ganesh Chandra Nayak *[a]

A quick and potent electrochemical etching of Ti_3AlC_2 at room temperature is developed. Studies reveal the purity of $Ti_3C_2T_x$ without any formation of TiO_2 or over-etching of MAX phase. The delaminated MXene was studied as all-solid-state flexible supercapacitor which performed better than the conventionally synthesized one.

MXenes are an interesting class of layered 2D transition metal carbides, nitrides, and/or carbonitrides discovered in 2011, hold unique combination of fascinating properties like hydrophilicity, high electrical conductivity, stability, light weight, and porosity.[1,2] They are generally described by $M_{n+1}X_nT_x$ (n = 1–4; M is transition metals; X is C and/or N; T_x is surface terminal groups including –F, –OH, –O, and/or –Cl).[3] Generally, MXenes are synthesized by selective elimination of A atoms from hexagonal layered MAX phase ($M_{n+1}AX_n$; A is mostly group 13 or 14 element) materials.[4] Among different synthesized MXenes, titanium carbide ($Ti_3C_2T_x$) and its composites have been gaining huge interest in wide range of areas including energy conversion and storage, catalysis, sensing, adsorption, field effect transistors, electromagnetic interference shielding, water purification, separation, lubrication, and photothermal conversion.[5–9]

Previous studies have shown that chemical etching is the most common method to prepare $Ti_3C_2T_x$ from Ti_3AlC_2.[1] The mechanism of chemical etching is dependent on the higher chemical reactivity of 'M–A' bond than 'M–C' bond and this is basically an electrochemical method.[10] Each surface active spots involves in both cathodic and anodic reaction during a usual chemical etching process. In case of electrochemical etching, the cathodic and anodic sites are isolated, and the etching reactions are operated by the bias.[11] According to previous studies, various electrolytes like HCl, NaCl, H_2SO_4, HNO_3, NH_4Cl, NaOH, and $FeCl_3$ have been used for the electrochemical etching of MAX phases including Ti_2AlC, V_2AlC, Cr_2AlC, and Ti_3AlC_2.[2] But, the atomically thin A layer elimination was not successful may be due to kinetic problems.[12] MAX phases either get over etched like both A and M layers get eliminated resulting carbide derived carbon, or only the M layer get etched resulting an AX like structure (for Ti_3SnC_2 and Ti_2SC).[13,14] In previous studies, compacted MAX phase block has been electrochemically etched and the etching reaction preferentially occurred on the surface.[2] It is usually difficult to obtain pure MXene sheets with complete etching which are generally obtained from chemical methods. But, chemical etching processes suffer from longer synthesis time like 2 to 3 days to obtain completely etched product often requiring higher temperatures.[15]

To overcome these limitations, in this study, MAX phase (Ti_3AlC_2) has been electrochemically etched by dispersing in the electrolyte (40% HF) with two platinum strips as electrodes. In contrast with the previously reported electrochemical etching methods, complete etching is obtained. Also, this process is much quicker than the commonly followed chemical etching methods. The completely etched MXene (EMX) is obtained within just 2 hours at room temperature and the quality of MXene sheets are comparable with the same obtained *via* chemical etching without any sheet breaking or formation of TiO_2. Moreover, the obtained $Ti_3C_2T_x$ is delaminated (named as d-EMX) using ionic liquid $[(Et_3HN)^+(NO_3)^-]$ and its capacitive performance as well as electrocatalytic activity is studied.

Electrochemical etching is carried out in a two-electrode set up keeping platinum strips as both positive and negative electrodes in HF electrolyte (Fig. 1a). The formation of AlF_3 during the etching in HF is generally a slow process. The reaction of Al with fluorine ions gets triggered in presence of applied potential which leads to a fast overall etching of $Ti_3C_2T_x$.[16] The overall electrochemical etching reaction is described as follows:[17] A comparison of previously reported electrochemical etching

[a] *Department of Chemistry and Chemical Biology, Indian Institute of Technology (ISM), Dhanbad-826004, Jharkhand, India. E-mail: gcnayak@iitism.ac.in*
[b] *P. G. Department of Chemistry, Berhampur University, Odisha 760007, India*

† Electronic supplementary information (ESI) available: Materials, characterization techniques, experimental procedures, XRD, FESEM, EDS, mapping of $Ti_3C_2T_x$, electrochemical performance of assembled supercapacitor device, and electrocatalytic activity of delaminated $Ti_3C_2T_x$ for OER and HER. See DOI: https://doi.org/10.1039/d3ya00489a

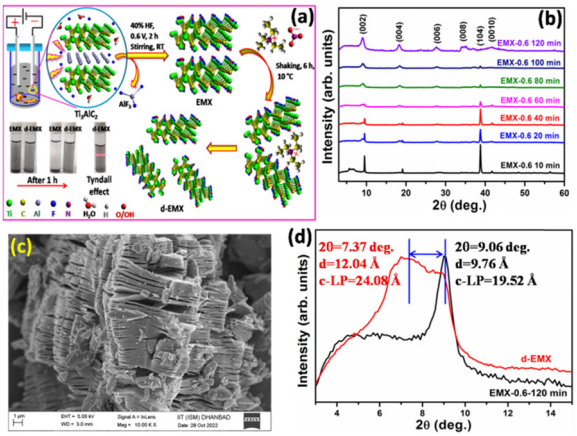

Fig. 1 (a) Schematic representation of electrochemical etching and delamination process with the stability study of EMX-0.6–120 min and d-EMX dispersion solution, (b) XRD spectra of synthesized EMX samples obtained after different time interval, (c) FESEM image of EMX-0.6–120 min, and (d) XRD spectra of EMX-0.6–120 min, and d-EMX.

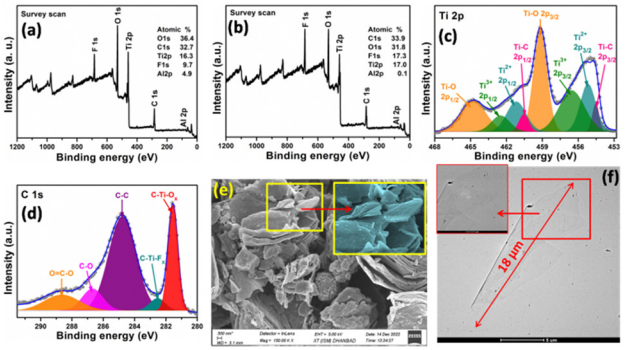

Fig. 2 XPS survey scan of (a) EMX-0.6–20 min, and (b) EMX-0.6–120 min with percentages of different atoms present; deconvoluted XPS spectra of (c) Ti 2p, and (d) C 1s; (e) FESEM image of d-EMX (inset shows zoomed image of a part of the FESEM image), (f) TEM image of d-EMX (inset shows magnified version of a part of the TEM image).

methods with this study are included in Table S1 (ESI†).

$$Ti_3AlC_2 + 5HF + 4H_2O \rightarrow Ti_3C_2F_2(OH)_2O_2 + \frac{11}{2}H_2 + AlF_3 \quad (1)$$

The etching time of the prepared $Ti_3C_2T_x$ is optimized using X-ray diffraction (XRD) analysis by varying the time from 10 to 120 minutes (Fig. 1b). The diffraction peak at $2\theta = 38.9^\circ$ associated with (104) plane of Al[6] reduces with increasing time and completely disappears after 120 min (2 hours). Further, the absence of TiO_2 plane in XRD, confirms no over-etching of the EMX sheets. The applied voltage was changed from 0.4 to 0.8 V, and no such change in the XRD pattern is observed (Fig. S1a, ESI†). The process is also useful to process large batches of MAX phase to prepare pure $Ti_3C_2T_x$ within 2 hours which is observed from XRD analysis (Fig. S1c, ESI†). Also, at the same reaction condition without the applied voltage, MAX phase cannot be completely etched (Fig. S1c, ESI†). The field emission scanning electron microscopy (FESEM) analysis (Fig. S2, S4 and S6, ESI†) shows distinct elimination of Al layer and formation of thin EMX sheets (Fig. 1c) with increasing etching time up to 2 hours. The disappearance of Al plane observed from XRD is well supported by the energy dispersive X-ray spectroscopy (EDS) analysis (Fig. S1d, S3, S5 and S7, ESI†) where the Al content gradually decreases with increasing etching time. From XRD, FESEM, and EDS analysis, it is confirmed that the complete etching is obtained within 2 hours with overall layer separation and low Al%.

Additionally, X-ray photoemission spectroscopy (XPS) (Fig. 2a and b) supports the above fact that the atomic percentage of aluminium present in EMX sample obtained after 2 hour of etching (EMX-0.6–120 min) is much lower than the EMX sample obtained after 20 minute of etching (EMX-0.6–20 min). Regarding the deconvoluted XPS analysis of EMX-0.6–120 min sample, its Ti 2p spectrum (Fig. 2c) shows four doublets of Ti $2p_{3/2}$ and Ti $2p_{1/2}$ with doublet gap of 5.9 eV and 2 : 1 area ratio, in accordance with prior XPS reports of pure $Ti_3C_2T_x$.[18,19] The peaks of Ti $2p_{3/2}$ for Ti–C, Ti^{2+}, Ti^{3+}, and Ti–O bond are observed at 454.5, 455.2, 456.5, and 459.2 eV, respectively. On the other hand, the peaks of Ti $2p_{1/2}$ for Ti–C, Ti^{2+}, Ti^{3+}, and Ti–O bond are observed at 460.5, 461.1, 462.5, and 464.7 eV, respectively.[18–20] In Fig. 2d, the core level C 1s XPS spectrum displays characteristic peaks at 281.5, 282.5, 284.8, 286.7, 287.6, and 288.6 eV associated with C–Ti–O_x, C–Ti–F_x, C–C, C–O, C═O, and O═C–O bonds, respectively.[21,22] Here, the presence of Ti–O, C–Ti–O, C–Ti–F, and C–O bonds indicate the surface functionality of $Ti_3C_2T_x$. It is observed that the peak positions for Ti 2p and C 1s in EMX-0.6–60 min (Fig. S9a and b, ESI†) and EMX-0.6–100 min (Fig. S9c and d, ESI†) are same as EMX-0.6–120 min. Thus, there is no indication of over etching or oxidation of Ti with increasing the etching time. As the Al layer gets removed from the MAX phase, the increment in surface functionality with increasing the etching time is indicated by increasing the peak area of C–Ti–O_x and C–Ti–F_x in C 1s spectrum. For the Raman spectrum (Fig. S1b, ESI†), the two peaks at 400, and 620 cm^{-1} are assigned to Ti–C vibrations.[23] The D and G bands at 1346, and 1567 cm^{-1}, respectively represent the molecular defects and in-plane sp^2 carbon atoms and the I_D/I_G ratio (0.78) reveals the ratio of disordered and amorphous carbon present in $Ti_3C_2T_x$ structure.[23]

The synthesized EMX-0.6–120 min is further delaminated with ionic liquid $[(Et_3HN)^+(NO_3)^-]$ for the first time. The ionic liquid is recovered after delamination and can be used further. After the addition of EMX into the ionic liquid, bulky $(Et_3HN)^+$ ions interact with the negatively charged EMX surface due to the presence of –F, –OH, –O functional groups. Further, shaking promotes delamination due to the insertion of bulky $(Et_3HN)^+$ ions inside overall EMX layers. The d-EMX suspension remains quite stable differently from the EMX (EMX-0.6–120 min) dispersion which is not stable more than 1 hour (Fig. 1a). Delamination of the sheets of EMX-0.6–120 min sample is supported by XRD analysis (Fig. 1d). The left shifting and broadening of (002) diffraction plane can be observed from $2\theta = 9.06^\circ$ of EMX to $2\theta = 7.37^\circ$ of d-EMX with increment of *d*-spacing and *c*-lattice parameter (*c*-LP) of 2.28 Å and 4.56 Å, respectively. The insertion

of bulky $(Et_3HN)^+$ group inside the stacked EMX layers disrupted the ordered stacking of the sheets resulting delaminated disordered sheets for d-EMX observed from the FESEM analysis (Fig. 2e). The d-EMX sheets can be clearly observed from Transmission Electron Microscopy (TEM) analysis (Fig. 2f). The transparent d-EMX sheets confirm the delamination using ionic liquid. The TEM elemental mapping exhibits the presence of C, Ti, F, and O (Fig. S8a–e, ESI†) which confirms the $Ti_3C_2T_x$ structure. The presence of bigger d-EMX sheets with diagonal length of ~18 μm indicates that shaking did not break the sheet during delamination which is much effective and useful method than the general delamination of MXene using sonication method.

After confirming the compositional, structural, and morphological properties, the electrochemical performance of d-EMX is studied by assembling all-solid-state flexible asymmetric supercapacitor device (ASSASC). The electrode preparation process is included in ESI† (Electrochemical study). As it is an established fact that $Ti_3C_2T_x$ is a good anode material,[24] we checked the electrochemical performance of d-EMX (Fig. S8f, ESI†) in three-electrode system *via* cyclic voltammetry (CV) analysis in both positive and negative voltage window using 1 M KOH electrolyte and much higher performance can be observed in negative voltage range indicating d-EMX a better anode material than cathode. Therefore, we use d-EMX as negative electrode and MnO_2 (purchased from SRL, India) which is a commercial cathode material is used as positive electrode for the two-electrode system. The device study was performed within a potential range of 0.0 to 0.8 V using PVA–KOH as separator as well as gel electrolyte. The PVA–KOH gel was first painted over the electrodes with the dimension of 2 cm × 3 cm and dried to assemble ASSASC device. Fig. 3(a) schematically represents the components of the ASSASC device. The active mass of the loaded electrode material is 10 mg. The ASSASC device exhibited a quasi rectangular CV curve (Fig. S10a, ESI†) at scan rates from 10 to 100 mV s^{-1} which indicates capacitive behavior of the sample. Similar trend is followed by the GCD analysis at different current densities from 1 to 3 A g^{-1} (Fig. S10b, ESI†). The device delivered specific capacitance, energy density, and power density of 162 F g^{-1}, 14.4 W h kg^{-1}, and 800 W kg^{-1}, respectively at 1 A g^{-1} current density. Notably, such high specific capacitance is surpasses those of the priorly reported chemically or electrochemically etched $Ti_3C_2T_x$ materials (Table S2, ESI†). The high specific capacitance is attributed to the proper etching without any oxidation of Ti atoms as well as effective delamination with few layered $Ti_3C_2T_x$ sheets.

Fig. 3b and c shows the CV analysis at 10 mV s^{-1} scan rate and galvanostatic charge–discharge (GCD) analysis at 1.5 A g^{-1}, respectively, at different bending angles like 0°, 60°, 90°, 120°, and 180° (Fig. 3d). A good flexibility and electrochemical stability is established for the assembled device as there is no obvious change can be observed from the CV and GCD curves under various bending states. The ASSASC device also exhibited long term cyclic life with 83.6% specific capacitance retention up to 10 000 cycles (Fig. 4a). Inset of Fig. 4a shows the Nyquist plot before and after the cyclic stability study. The pore blockage and the degradation of the PVA–KOH separator during

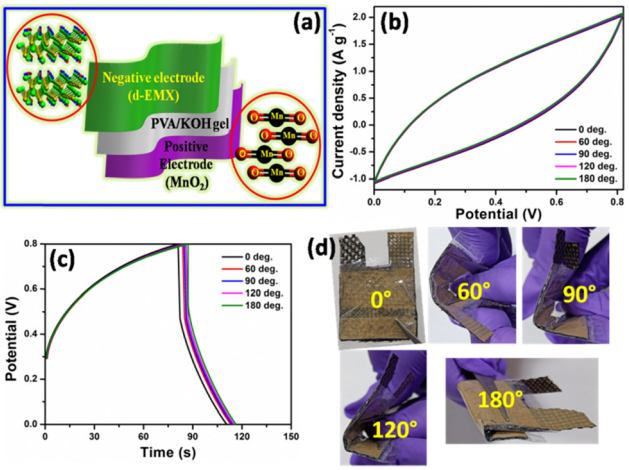

Fig. 3 (a) Schematic illustration of the different components of fabricated ASSASC device, (b) CV, and (c) GCD profiles of the ASSASC device at different bending states, (d) digital pictures of the assembled ASSASC device at different bending angles.

continuous charge–discharge lead to the increment in solution resistance and thus the decrease in cyclic life. However, decrease in charge transfer resistance after the cyclic stability study indicates that there is increased amount of electrolyte access on the surface of the electrode.[25,26] FESEM image (Fig. S10c, ESI†) reveals that the structural morphology of d-EMX remains quite stable after the stability study. Further, the Ragone plot (Fig. 4b) revealed that the energy density of our device is much higher than that of the previously reported MXene based devices (+//−) including $Ti_3C_2T_x$/N-doped carbon foam//$Ti_3C_2T_x$/N-doped carbon foam (8.75 W h kg^{-1}),[27] reduced graphene oxide//$Ti_3C_2T_x$ (8 W h kg^{-1}),[28] $Ti_3C_2T_x$/carbon fibre//$Ti_3C_2T_x$/carbon fibre (10.6 W h kg^{-1}),[29] and $Ti_3C_2T_x$//activated carbon (5.5 W h kg^{-1}).[30] From these characteristic electrochemical performances, it can be concluded that d-EMX can be used as an efficient anode material for supercapacitor application.

The practical applicability of the assembled ASSASC device is further studied by connecting three devices in series and

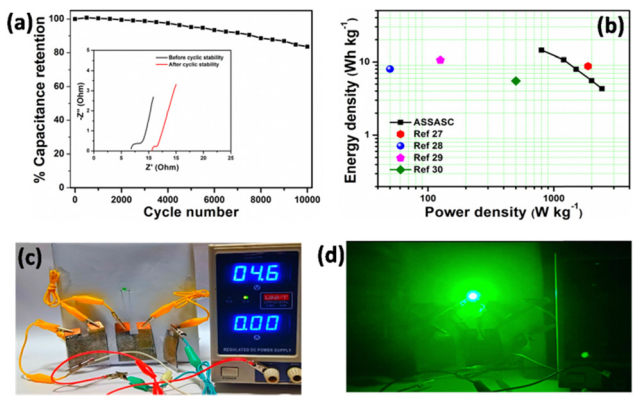

Fig. 4 (a) Cyclic stability study of the ASSASC device (inset Nyquist plots before and after the cyclic stability study), (b) Ragone plot of the device comparing with some prior reported results; digital picture of (c) charging setup three ASSASC devices connected in series, and (d) glowing a green LED.

Fig. 4c shows the charging set-up. The assembled devices are able to brightly glow a 3 V green LED shown in Fig. 4d. Fig. S10e and f (ESI†) show that bending does not affect the practical applicability of the devices.

MXenes are increasingly appealing for their interesting electrocatalytic property.[31,32] Here, the bifunctional electrocatalytic property of d-EMX is also studied as full water-splitting catalyst. OER and HER activities of the sample are carried out in 1 M KOH and 1 M H_2SO_4 electrolyte, respectively. The LSV curves for OER and HER at different scan rates (5, 10, and 50 mV s^{-1}) are shown in Fig. S11a and b (ESI†). The LSV study of d-EMX at 50 mV s^{-1} (Fig. S11a, ESI†) exhibits a low onset potential of 1.45 V *vs.* RHE for OER performance. In case of HER study, the LSV curve of d-EMX at 50 mV s^{-1} (Fig. S11b, ESI†) shows a low onset potential of −0.19 V *vs.* RHE. These results are much superior than that of previously reported MXene based electrocatalysts (Table S3, ESI†). These catalytic performances suggest that d-EMX can be an efficient bifunctional electrocatalyst for overall water–splitting.

In summary, we have demonstrated a quick strategy to synthesize $Ti_3C_2T_x$ from Ti_3AlC_2 *via* electrochemical etching method. By optimizing the applied voltage and time $Ti_3C_2T_x$ can be synthesized only in 2 hours without any over-etching or oxidation of Ti atoms. The obtained MXene was successfully delaminated to few layered sheets with bigger sheet length using $[(Et_3HN)^+(NO_3)^-]$ ionic liquid for the first time *via* shaking. The delaminated MXene delivered superior specific capacitance of 162 F g^{-1} at 1 A g^{-1} while assembled as all-solid-state asymmetric supercapacitor. The fabricated device was highly flexible with no obvious change in electrochemical performance under different bending angles. Additionally, the electrocatalytic performance of the delaminated MXene was also studied as bifunctional electrocatalyst for over-all water splitting and it exhibited good electrocatalytic activity in OER and HER. Therefore, this work paves a way to rapid bulk synthesis of MXene for commercial energy storage and conversion applications.

The IIT (ISM), Dhanbad provided research funds (Project No: IIT(ISM)/2023-2024/1001/INSTITUTE), a lab, central research facilities, and fellowship, which the authors gratefully acknowledge.

Conflicts of interest

There are no conflicts to declare.

Notes and references

1 W. Sun, S. Shah, Y. Chen, Z. Tan, H. Gao, T. Habib, M. Radovic and M. Green, *J. Mater. Chem. A*, 2017, **5**, 21663–21668.
2 S. Yang, P. Zhang, F. Wang, A. G. Ricciardulli, M. R. Lohe, P. W. Blom and X. Feng, *Angew. Chem.*, 2018, **130**, 15717–15721.
3 B. Anasori, M. R. Lukatskaya and Y. Gogotsi, *Nat. Rev. Mater.*, 2017, **2**, 1–17.
4 A. VahidMohammadi, A. Hadjikhani, S. Shahbazmohamadi and M. Beidaghi, *ACS Nano*, 2017, **11**, 11135–11144.
5 S.-Y. Pang, Y.-T. Wong, S. Yuan, Y. Liu, M.-K. Tsang, Z. Yang, H. Huang, W.-T. Wong and J. Hao, *J. Am. Chem. Soc.*, 2019, **141**, 9610–9616.
6 C. Cui, M. Hu, C. Zhang, R. Cheng, J. Yang and X. Wang, *Chem. Commun.*, 2018, **54**, 8132–8135.
7 M. Zhu, Y. Huang, Q. Deng, J. Zhou, Z. Pei, Q. Xue, Y. Huang, Z. Wang, H. Li and Q. Huang, *Adv. Energy Mater.*, 2016, **6**, 1600969.
8 L. Huang, L. Ding, J. Caro and H. Wang, *Angew. Chem., Int. Ed.*, 2023, e202311138.
9 L. Huang, L. Ding and H. Wang, *Small Sci.*, 2021, **1**, 2100013.
10 P. Srivastava, A. Mishra, H. Mizuseki, K.-R. Lee and A. K. Singh, *ACS Appl. Mater. Interfaces*, 2016, **8**, 24256–24264.
11 V. Naguib and M. Mochalin, *Adv. Mater.*, 2014, **26**, 992.
12 T. Li, L. Yao, Q. Liu, J. Gu, R. Luo, J. Li, X. Yan, W. Wang, P. Liu and B. Chen, *Angew. Chem., Int. Ed.*, 2018, **57**, 6115–6119.
13 M. R. Lukatskaya, J. Halim, B. Dyatkin, M. Naguib, Y. S. Buranova, M. W. Barsoum and Y. Gogotsi, *Angew. Chem.*, 2014, **126**, 4977–4980.
14 M. Q. Zhao, M. Sedran, Z. Ling, M. R. Lukatskaya, O. Mashtalir, M. Ghidiu, B. Dyatkin, D. J. Tallman, T. Djenizian and M. W. Barsoum, *Angew. Chem.*, 2015, **127**, 4892–4896.
15 M. Benchakar, L. Loupias, C. Garnero, T. Bilyk, C. Morais, C. Canaff, N. Guignard, S. Morisset, H. Pazniak and S. Hurand, *Appl. Surf. Sci.*, 2020, **530**, 147209.
16 X. Zhang and T. Devine, *J. Electrochem. Soc.*, 2006, **153**, B375.
17 S. De, S. Acharya, S. Sahoo and G. C. Nayak, *Mater. Chem. Front.*, 2021, **5**, 7134–7169.
18 W. Y. Chen, X. Jiang, S.-N. Lai, D. Peroulis and L. Stanciu, *Nat. Commun.*, 2020, **11**, 1–10.
19 R. B. Rakhi, B. Ahmed, M. N. Hedhili, D. H. Anjum and H. N. Alshareef, *Chem. Mater.*, 2015, **27**, 5314–5323.
20 Y. T. Liu, P. Zhang, N. Sun, B. Anasori, Q. Z. Zhu, H. Liu, Y. Gogotsi and B. Xu, *Adv. Mater.*, 2018, **30**, 1707334.
21 X. Li, X. Yin, M. Han, C. Song, H. Xu, Z. Hou, L. Zhang and L. Cheng, *J. Mater. Chem. C*, 2017, **5**, 4068–4074.
22 R. P. Raj, P. Ragupathy and S. Mohan, *J. Mater. Chem. A*, 2015, **3**, 24338–24348.
23 S. Shen, T. Ke, K. Rajavel, K. Yang and D. Lin, *Small*, 2020, **16**, 2002433.
24 S. De, C. K. Maity, S. Sahoo and G. C. Nayak, *ACS Appl. Energy Mater.*, 2021, **4**, 3712–3723.
25 Y. Wang, L. Liu, Y. Wang, J. Qu, Y. Chen and J. Song, *ACS Nano*, 2023, **17**, 21761–21770.
26 Y. Wang, J. Song and W. Y. Wong, *Angew. Chem.*, 2023, **135**, e202218343.
27 L. Sun, G. Song, Y. Sun, Q. Fu and C. Pan, *ACS Appl. Mater. Interfaces*, 2020, **12**, 44777–44788.
28 A. M. Navarro-Suárez, K. L. Van Aken, T. Mathis, T. Makaryan, J. Yan, J. Carretero-González, T. Rojo and Y. Gogotsi, *Electrochim. Acta*, 2018, **259**, 752–761.
29 L. Sun, Q. Fu and C. Pan, *J. Hazard. Mater.*, 2021, **410**, 124565.
30 T.-H. Chang, T. Zhang, H. Yang, K. Li, Y. Tian, J. Y. Lee and P.-Y. Chen, *ACS Nano*, 2018, **12**, 8048–8059.
31 A. Liu, X. Liang, X. Ren, W. Guan, M. Gao, Y. Yang, Q. Yang, L. Gao, Y. Li and T. Ma, *Adv. Funct. Mater.*, 2020, **30**, 2003437.
32 L. Xiu, Z. Wang, M. Yu, X. Wu and J. Qiu, *ACS Nano*, 2018, **12**, 8017–8028.